Monthly Notices
of the
ROYAL ASTRONOMICAL SOCIETY

MNRAS **478,** 1502–1511 (2018)
Advance Access publication 2018 May 1

doi:10.1093/mnras/sty1099

OH^+ emission from cometary knots in planetary nebulae

F. D. Priestley★ and M. J. Barlow

Department of Physics and Astronomy, University College London, Gower Street, London WC1E 6BT, UK

Accepted 2018 April 24. Received 2018 March 23; in original form 2018 January 18

ABSTRACT

We model the molecular emission from cometary knots in planetary nebulae (PNe) using a combination of photoionization and photodissociation region (PDR) codes, for a range of central star properties and gas densities. Without the inclusion of ionizing extreme ultraviolet (EUV) radiation, our models require central star temperatures T_* to be near the upper limit of the range investigated in order to match observed H_2 and OH^+ surface brightnesses consistent with observations – with the addition of EUV flux, our models reproduce observed OH^+ surface brightnesses for $T_* \geq 100$ kK. For $T_* < 80$ kK, the predicted OH^+ surface brightness is much lower, consistent with the non-detection of this molecule in PNe with such central star temperatures. Our predicted level of H_2 emission is somewhat weaker than commonly observed in PNe, which may be resolved by the inclusion of shock heating or fluorescence due to UV photons. Some of our models also predict ArH^+ and HeH^+ rotational line emission above detection thresholds, despite neither molecule having been detected in PNe, although the inclusion of photodissociation by EUV photons, which is neglected by our models, would be expected to reduce their detectability.

Key words: astrochemistry – ISM: molecules – planetary nebulae: general.

1 INTRODUCTION

Planetary nebulae (PNe) are the end-stage of the life cycle of low- and intermediate-mass stars, consisting of the gas ejected during previous phases of stellar evolution, surrounding a hot central star. Following the discovery of CO and H_2 emission from PNe (Mufson, Lyon & Marionni 1975; Treffers et al. 1976), surveys have established that both molecules are commonly present in PNe (e.g. Huggins et al. 1996; Hora, Latter & Deutsch 1999), with the molecular gas component in some cases forming a significant fraction of the total nebular mass. Other molecules, such as HCN, HCO^+, and CS, have also been detected in PNe (Edwards, Cox & Ziurys 2014; Schmidt & Ziurys 2016), allowing investigation of the otherwise undetectable neutral regions.

In order to survive the ultraviolet (UV) radiation from the central star, molecules must be shielded within regions with significant optical depths (Tielens & Hollenbach 1993; Natta & Hollenbach 1998), such as the cometary knots commonly observed in PNe (O'Dell & Handron 1996; O'Dell et al. 2002). Matsuura et al. (2009) found that the H_2 emission from NGC 7293 is highly localized within these knots, although in NGC 6781 the molecular emission more resembles a ring surrounding the central star (Bachiller et al. 1993; Hiriart 2005). Aleman et al. (2011) were able to reproduce the observed H_2 surface brightnesses of cometary knots in NGC 7293 with a combined photoionization/photodissociation region (PDR) code, finding that the low-density/diffuse gas surrounding the knots contributes very little to the overall H_2 emission. A detailed model of NGC 6781, assuming a dense, shock-heated PDR surrounding the inner ionized region, was produced by Otsuka et al. (2017) to fit a wide range of observational data from the UV to radio, including H_2 and CO molecular emission.

The molecular ion OH^+, originally observed in emission around ultraluminous galaxies (van der Werf et al. 2010), in the interstellar medium (ISM; Wyrowski et al. 2010), the Orion bar (van der Tak et al. 2013) and, along with ArH^+, in the Crab nebula (Barlow et al. 2013), was detected in five PNe by Etxaluze et al. (2014) and Aleman et al. (2014). Aleman et al. (2014) noted that all five PNe had central star temperatures greater than 100 kK, and suggested that soft X-rays may be responsible for producing this emission, as in the case of ultraluminous galaxies (van der Werf et al. 2010). X-rays were also found to be needed to reproduce the observed abundances of CN and HCO^+ (Kimura, Gruenwald & Aleman 2012) in PNe. In their model of NGC 6781, Otsuka et al. (2017) predicted a significantly larger quantity of OH^+ than deduced from observations, despite good agreement with other molecular abundances.

In this paper, we model the molecular emission from cometary knots in PNe using a combination of photoionization and PDR codes. Previous efforts (Aleman & Gruenwald 2004; Aleman et al. 2011; Kimura et al. 2012; Otsuka et al. 2017) have treated both problems simultaneously, ensuring that the PDRs are modelled self-consistently by solving the full radiative transfer problem throughout the knot. We use the approach adopted by Priestley, Barlow & Viti (2017) for their Crab nebula modelling, assuming that the

---

★ E-mail: fdp@star.ucl.ac.uk

Published by Oxford University Press on behalf of the Royal Astronomical Society

Table 1. Gas-phase elemental abundances, relative to hydrogen, adopted for the PN modelling.

Element	Abundance	Element	Abundance
H	1.00	Mg	1.5×10^{-6}
He	0.10	Si	1.5×10^{-6}
C	2.5×10^{-4}	S	1.5×10^{-5}
N	1.0×10^{-4}	Cl	1.8×10^{-7}
O	5.0×10^{-4}	Ar	2.0×10^{-6}
Ne	1.0×10^{-4}	Fe	1.5×10^{-7}

photoionized region can be modelled separately from the PDR, providing an incident radiation field which determines the properties of the neutral gas. This allows us to use more detailed PDR models, including more molecular species and calculating the emission self-consistently, and to investigate a larger range of parameter space, due to the lower computational cost. Rather than attempt to reproduce the properties of one specific object, we vary the input parameters of our models and compare the resulting molecular emission predictions to the values typically observed in PNe.

2 METHOD

To determine the incident radiation field on the knots, we model the photoionized region of the PNe using MOCASSIN (Ercolano et al. 2003; Ercolano, Barlow & Storey 2005; Ercolano et al. 2008), a Monte Carlo photoionization code. We assume a 1D spherically symmetric geometry, with an inner region of diffuse gas of density n_d extending up to a radius r_k at which the knot is located, beyond which the gas density is increased to n_k. We increase the width of this dense region until the ionizing extreme ultraviolet (EUV) flux (taken to be 200−912 Å) has been fully absorbed, marking the transition from a photoionized region to a PDR. We then integrate the emerging spectral energy distribution (SED) from 912 to 2400 Å to determine the far-UV (FUV) field (in Draine units, ∼1.7 times the Habing field; Habing 1968; Draine 1978) and from 0.1 to 200 Å to determine the X-ray flux incident on the PDR. We then model the PDR as a 1D slab with constant density n_k and a thickness of Δr_k using UCL_PDR (Bell et al. 2005, 2006; Bayet et al. 2011; Priestley et al. 2017), a PDR code that is also capable of treating X-rays. We assume Δr_k is small enough compared to r_k that we can ignore the effect of geometrical dilution on the radiation field inside the PDR. We take $n_d = 100\,\mathrm{cm}^{-3}$, at the lower end of the typical density range of $10^2-10^4\,\mathrm{cm}^{-3}$ for diffuse gas in PNe (Osterbrock & Ferland 2006), and $n_k = 10^5\,\mathrm{cm}^{-3}$, appropriate for the cometary knots in NGC 7293 (Meaburn et al. 1998; Matsuura et al. 2007). We use $r_k = 0.2$ pc and $\Delta r_k = 0.003$ pc, again consistent with values for the cometary knots in NGC 7293 (Matsuura et al. 2009).

The gas-phase elemental abundances used are listed in Table 1. We used values typical of PNe (Kingsburgh & Barlow 1994; Pottasch, Beintema & Feibelman 2005), with the exception of Mg, Si, and Fe, where we assumed solar abundances (Lodders 2010) depleted by the maximum ISM values from Jenkins (2009). We assumed a dust-to-gas mass ratio of 0.005, typical of values found for PNe (Aleman et al. 2011; Ueta et al. 2014; Otsuka et al. 2017). We used a dust composition of half amorphous carbon, half silicate grains and a power-law grain size distribution with an exponent of −3.5, and minimum/maximum grain radii of 0.005/0.25μm. The choice of grain composition has been found to have only a small effect on H_2 abundances and emission – while the dust-to-gas mass ratio and dust grain size can cause significant variations (Aleman & Gruenwald 2004, 2011; Aleman et al. 2011), we do not investigate varying the dust properties in our models.

We investigate central star luminosities of $L_* = 100$ and $1000\,\mathrm{L}_\odot$, and temperatures of $T_* = 50$, 80, 100, 120, and 150 kK, covering much of the parameter space relevant to old PNe (Vassiliadis & Wood 1994; Miller Bertolami 2016). We used model stellar spectra from the TheoSSA data base (Rauch 2003), using $\log g = 6.0$, 7.0, and 8.0 as typical values for PNe without stellar winds or outflows (Guerrero & De Marco 2013), and take $\log g = 7.0$ as our standard value. We found that the transmitted X-ray SED output from our MOCASSIN models could be well fitted by a four-component power law. The transmitted UV and X-ray fluxes for each combination of L_*, T_*, and $\log g$ are listed in Table 2.

For our PDR modelling, we used the chemical network from Priestley et al. (2017), including ArH^+ and HeH^+. We use the dissociative recombination rate for ArH^+ with electrons calculated by Abdoulanziz et al. (in preparation). We included the collisional excitation of OH^+ by H using the rate coefficients calculated by Lique, Bulut & Roncero (2016), which may become important in lower ionization regions, in addition to collisional excitation by electrons (van der Tak et al. 2013). We assume a typical ISM value for the cosmic ray ionization rate ($1.3 \times 10^{-17}\,\mathrm{s}^{-1}$) and an A_V/N_H conversion factor of $3.0 \times 10^{-22}\,\mathrm{mag\,cm}^2$, reduced from ISM values by a factor of 2 to account for our lower dust-to-gas mass ratio. Values of the cosmic ray ionization rate derived from observations can be higher than our adopted value by over an order of magnitude (e.g. Neufeld & Wolfire 2017), which may become important if the ionization rate exceeds that from the X-ray flux.

We also investigate the likely effects of the EUV (200−912 Å) flux, suggested to be responsible for powering H_2 emission in NGC 7293 by O'Dell, Henney & Ferland (2007), by running MOCASSIN models consisting of only diffuse gas up to r_k, without the denser shell absorbing the ionizing radiation. The transmitted fluxes are listed in Table 3. The 'X-ray' fluxes, now defined as over the wavelength range 0.1–750 Å, are significantly increased for all models, and are much less affected by T_*, as the expanded range includes the SED peak for all central star temperatures. The UV fields are slightly reduced from the previous values, as the diffuse UV emission from the dense ionized gas (calculated in MOCASSIN but not UCL_PDR) is no longer included. UCL_PDR treats X-rays following the methods described in Meijerink & Spaans (2005) – the extent to which this approach is valid for EUV photons, and the likely impact on our results, is discussed in Section 4.2.

3 RESULTS

Fig. 1 shows the predicted OH^+ 971 GHz line surface brightness versus T_*, for models with $\log g = 7.0$. The emission strength increases rapidly for central star temperatures above 100 kK, while also increasing with L_*, as increasing X-ray fluxes enhance the ionized fraction in the gas and thus the OH^+ abundance (van der Werf et al. 2010). The observed range of surface brightnesses (Aleman et al. 2014; Etxaluze et al. 2014) can be explained by models with central star temperatures close to 150 kK, although these models have OH^+ column densities in excess of the values calculated by Aleman et al. (2014). For $T_* \leq 120$ kK, the surface brightnesses are well below those observed, despite several PNe with OH^+ detections having central star temperatures in this region. The line ratios between the three lowest frequency OH^+ rotational transitions, at 909, 971, and 1033 GHz, are essentially constant across all models, with relative strengths of 0.2:1:0.6, respectively. This is in qualitative agreement with the ratios for all the PNe with detected OH^+ emission, from

Table 2. Central star luminosities L_* and effective temperatures T_*, and output UV and X-ray fluxes from our MOCASSIN modelling of PNe. The X-ray component includes all transmitted flux between 0.1 and 200 Å.

		$\log g = 7.0$		$\log g = 6.0$		$\log g = 8.0$	
$L_*/L_\odot$	T_*/kK	F_{UV}/Draines	F_X/ erg cm^{-2} s^{-1}	F_{UV}/Draines	F_X/ erg cm^{-2} s^{-1}	F_{UV}/Draines	F_X/ erg cm^{-2} s^{-1}
10^2	50	233	0.00	226	0.00	238	0.00
10^2	80	91.5	3.24×10^{-7}	92.9	3.67×10^{-7}	90.6	3.73×10^{-7}
10^2	100	69.8	2.18×10^{-5}	71.5	7.31×10^{-5}	68.7	4.96×10^{-6}
10^2	120	59.2	6.56×10^{-4}	60.0	2.32×10^{-3}	58.8	4.04×10^{-4}
10^2	150	48.1	4.55×10^{-2}	47.2	6.16×10^{-2}	48.7	3.52×10^{-2}
10^3	50	2230	0.00	2160	0.00	2280	0.00
10^3	80	817	1.05×10^{-6}	829	1.01×10^{-6}	815	2.13×10^{-6}
10^3	100	606	2.39×10^{-4}	622	8.61×10^{-4}	596	5.75×10^{-5}
10^3	120	501	7.38×10^{-3}	499	4.19×10^{-2}	497	4.43×10^{-3}
10^3	150	366	0.570	351	0.713	377	0.459

Table 3. Central star luminosities L_* and effective temperatures T_*, and output UV and X-ray fluxes from our MOCASSIN modelling of PNe, for model atmospheres with $\log g = 7.0$ including the EUV flux. The X-ray component now includes all flux up to 750 Å.

L_* / $L_\odot$	T_* / kK	F_{UV} / Draines	F_X / erg cm^{-2} s^{-1}
10^2	50	233	0.183
10^2	80	85.1	0.550
10^2	100	62.7	0.605
10^2	120	51.7	0.613
10^2	150	41.7	0.580
10^3	50	2110	6.54
10^3	80	609	11.8
10^3	100	387	12.6
10^3	120	284	12.4
10^3	150	175	13.4

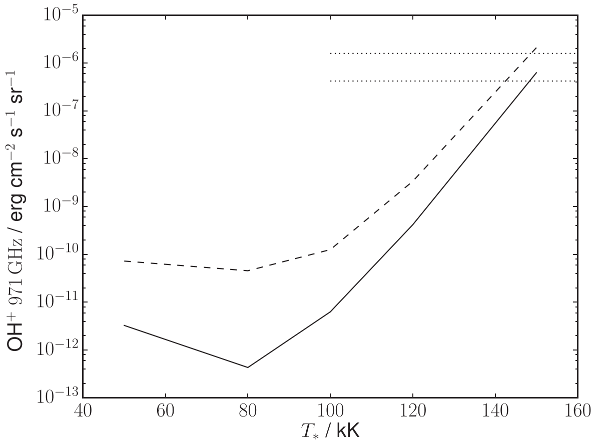

Figure 1. OH$^+$ 971 GHz surface brightness versus T_*, for models with $n_H = 10^5$ cm^{-3}, $\log g = 7.0$ and $L_* = 100\,L_\odot$ (solid line) and $1000\,L_\odot$ (dashed line). The dotted horizontal lines show the range of observed values from Etxaluze et al. (2014) and Aleman et al. (2014).

Aleman et al. (2014) and Etxaluze et al. (2014), with the exception of NGC 6781.

Fig. 2 shows the predicted H_2 2.12 µm line surface brightness versus T_* for two values of the central star luminosity. The range of values observed in PNe from Hora et al. (1999) is also shown. The predicted emission strength is barely affected by L_*, and is roughly constant below 120 kK, as the H_2 line requires significant population of the $v = 1$ vibrational state, and the PDR gas temperature is far higher for the 150 kK models than for those with lower T_*. For $T_* = 150$ kK, the predicted H_2 surface brightnesses are consistent with the smallest values detected by Hora et al. (1999), but the highest surface brightnesses in this line are not reproduced by these models.

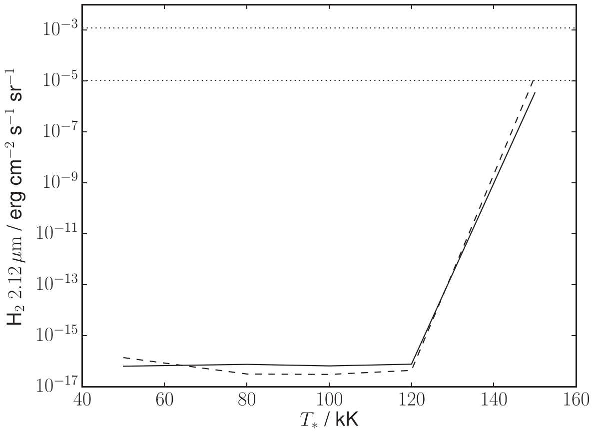

Figure 2. H_2 2.12 µm surface brightness versus T_*, for models with $n_H = 10^5$ cm^{-3}, $\log g = 7.0$ and $L_* = 100\,L_\odot$ (solid line) and $1000\,L_\odot$ (dashed line). The dotted horizontal lines show the range of observed values from Hora et al. (1999).

Fig. 3 shows the predicted CO J = 4−3 line surface brightness versus T_*. In this case, the emission is strongly affected by the value of L_*, as the increased UV field for the $1000\,L_\odot$ models readily dissociates CO molecules. Surface brightness increases with T_* for the same L_* as less of the central star flux is emitted at FUV wavelengths. The $100\,L_\odot$, 150 kK model has a predicted surface brightness comparable with the lowest values measured by Etxaluze et al. (2014) and Ueta et al. (2014), but again, no model reproduces the higher observed values. Increasing the elemental abundance of carbon is unlikely to resolve this discrepancy, as our oxygen abundance is only a factor of 2 higher, limiting the amount of CO which can be formed. Elemental oxygen abundances in PNe are rarely significantly higher than our value of 5×10^{-4} (Kingsburgh & Barlow 1994).

Fig. 4 shows the predicted ArH$^+$ J = 1–0 617 GHz line surface brightness versus T_*. ArH$^+$ has not been detected in any PN to date, despite the J = 1–0 and 2–1 transitions falling within the *Herschel* SPIRE frequency range. The dashed line in Fig. 4 corresponds to the surface brightness of the weakest OH$^+$ SPIRE line detection from Aleman et al. (2014). If this is taken as a lower limit, only the

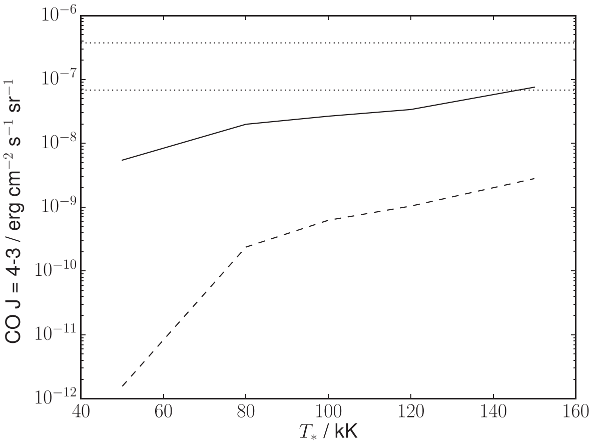

Figure 3. CO J = 4–3 surface brightness versus T_*, for models with $n_{\mathrm{H}} = 10^5$ cm^{-3}, $\log g = 7.0$, and $L_* = 100\,\mathrm{L}_\odot$ (solid line) and $1000\,\mathrm{L}_\odot$ (dashed line). The dotted horizontal lines show the range of observed values from Etxaluze et al. (2014) and Ueta et al. (2014).

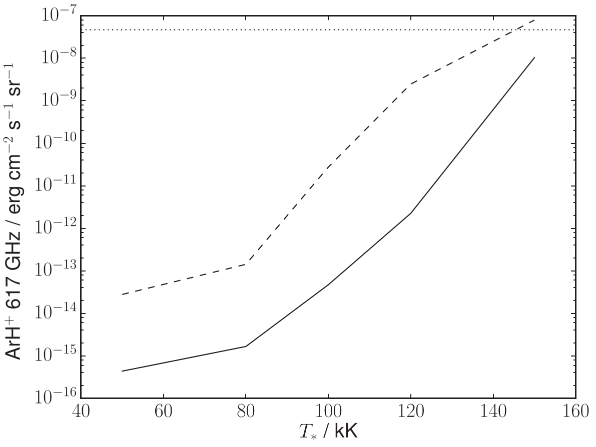

Figure 4. ArH$^+$ 617 GHz surface brightness versus T_*, for models with $n_{\mathrm{H}} = 10^5$ cm^{-3}, $\log g = 7.0$, and $L_* = 100\,\mathrm{L}_\odot$ (solid line) and $1000\,\mathrm{L}_\odot$ (dashed line). The dotted horizontal line shows the surface brightness of the weakest SPIRE OH$^+$ detection from Aleman et al. (2014).

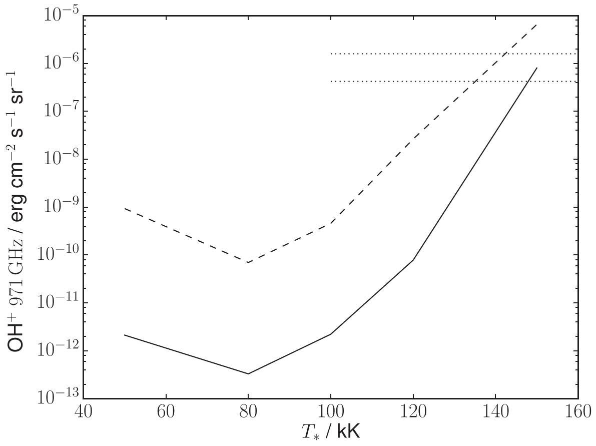

Figure 5. OH$^+$ 971 GHz surface brightness versus T_*, for models with $n_{\mathrm{H}} = 10^6$ cm^{-3}, $\log g = 7.0$ and $L_* = 100\,\mathrm{L}_\odot$ (solid line) and $1000\,\mathrm{L}_\odot$ (dashed line). The dotted horizontal lines show the range of observed values from Etxaluze et al. (2014) and Aleman et al. (2014).

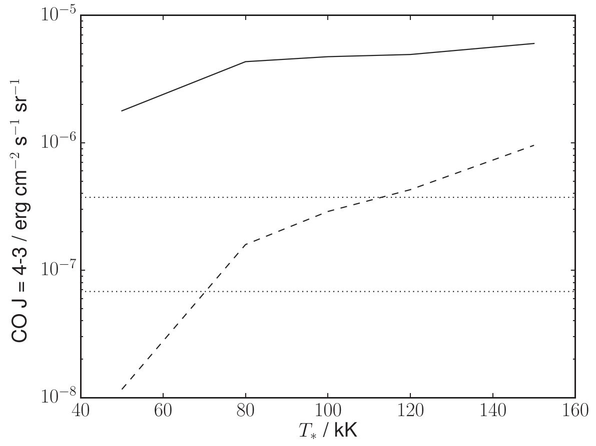

Figure 6. CO J = 4–3 surface brightness versus T_*, for models with $n_{\mathrm{H}} = 10^6$ cm^{-3}, $\log g = 7.0$, and $L_* = 100\,\mathrm{L}_\odot$ (solid line) and $1000\,\mathrm{L}_\odot$ (dashed line). The dotted horizontal lines show the range of observed values from Etxaluze et al. (2014) and Ueta et al. (2014).

150 kK, $1000\,\mathrm{L}_\odot$ model predicts detectable ArH$^+$ emission in this line, although the 150 kK, $100\,\mathrm{L}_\odot$ model is only a factor of a few below the limit. The J = 2–1 transition at 1234 GHz is generally brighter in all models by a factor of a few, but considering the lower signal-to-noise at higher frequencies, we still find only the 150 kK, $1000\,\mathrm{L}_\odot$ model produces a surface brightness above the weakest OH$^+$ (1033 GHz) line detection. A similar situation is found for the HeH$^+$ 149 μm line, using the OH$^+$ 152 μm PACS detections as a lower limit for detectability – all models except for 150 kK, $1000\,\mathrm{L}_\odot$ are below the detection threshold.

Increasing the gas density to $n_{\mathrm{H}} = 10^6$ cm^{-3}, while reducing Δr_k to 3×10^{-4} pc to ensure the same column density, the OH$^+$ and H_2 line surface brightnesses are increased for all models, with the effect greater for $L_* = 1000\,\mathrm{L}_\odot$. Fig. 5 shows the OH$^+$ 971 GHz line surface brightness versus T_*, for these increased density models. Even for $1000\,\mathrm{L}_\odot$, the increase in surface brightness is not great enough to bring models with $T_* < 150$ kK within the range of observed values. The CO J = 4–3 emission, shown in Fig. 6, is much more strongly affected, with all the $100\,\mathrm{L}_\odot$ models now exceeding the observational upper limits, while for $L_* = 1000\,\mathrm{L}_\odot$ the predicted surface brightnesses are comparable to observation, with the exception of the 50 kK model, for which it is still too low. ArH$^+$ and HeH$^+$ surface brightnesses both decrease, although the 150 kK, $1000\,\mathrm{L}_\odot$ model still predicts detectable levels for both molecules.

Fig. 7 shows the input stellar spectra for model atmospheres with $T_* = 120$ kK and $\log g$ ranging from 6.0 to 8.0, demonstrating the large variation at X-ray wavelengths between the models (note that the total flux up to 200 Å is highest for $\log g = 6.0$, despite F_λ being much lower at the shortest wavelengths). The results from our photoionization modelling, listed in Table 2, show that the incident X-ray flux is generally higher for $\log g = 6.0$ and lower for $\log g = 8.0$, while the UV field is not significantly affected.

Fig. 8 shows the OH$^+$ 971 GHz line surface brightness versus T_*, for models with $\log g = 6.0$. The increased X-ray flux results in stronger OH$^+$ emission, particularly for $T_* = 120$ kK, for which the $1000\,\mathrm{L}_\odot$ model gives a surface brightness within a factor of a few of observations. This model also predicts H_2 surface brightnesses consistent with observed values, compared to the $\log g = 7.0$ case, where the emission is far weaker. The CO J = 4–3 surface brightnesses are largely unchanged from the $\log g = 7.0$ case, while

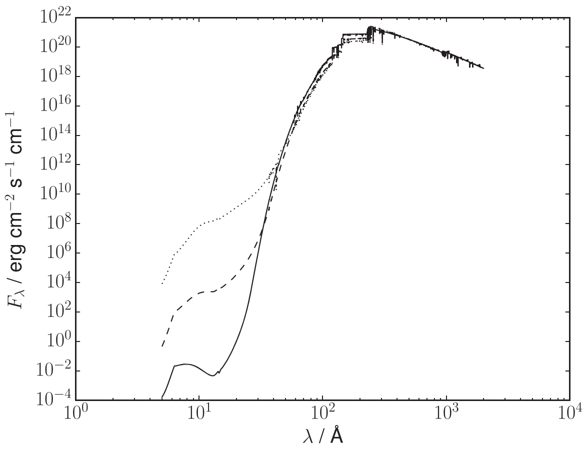

Figure 7. Model central star spectra for model atmospheres with $T_* = 120\,\mathrm{kK}$ and $\log g = 6.0$ (solid line), 7.0 (dashed line), and 8.0 (dotted line), obtained from the TheoSSA data base (Rauch 2003).

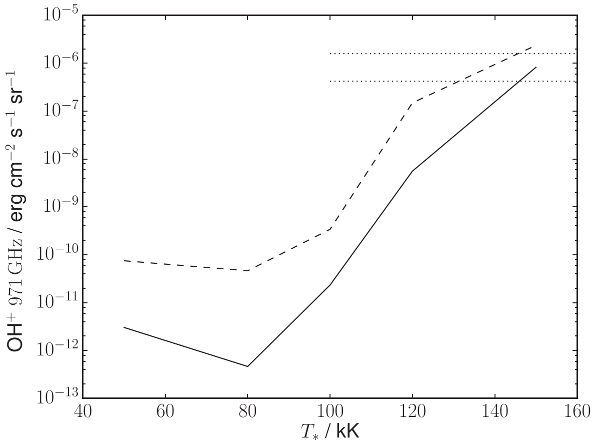

Figure 8. OH$^+$ 971 GHz surface brightness versus T_*, for models with $n_\mathrm{H} = 10^5\,\mathrm{cm}^{-3}$, $\log g = 6.0$, and $L_* = 100\,\mathrm{L}_\odot$ (solid line) and $1000\,\mathrm{L}_\odot$ (dashed line). The dotted horizontal lines show the range of observed values from Etxaluze et al. (2014) and Aleman et al. (2014).

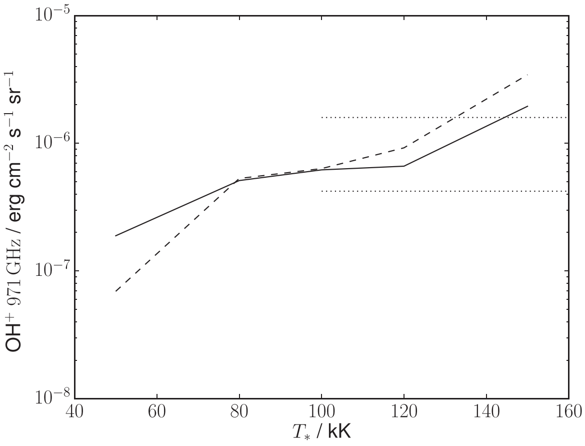

Figure 9. OH$^+$ 971 GHz surface brightness versus T_*, for models with $n_\mathrm{H} = 10^5\,\mathrm{cm}^{-3}$, $\log g = 7.0$, and $L_* = 100\,\mathrm{L}_\odot$ (solid line) and $1000\,\mathrm{L}_\odot$ (dashed line) including the EUV flux. The dotted horizontal lines show the range of observed values from Etxaluze et al. (2014) and Aleman et al. (2014).

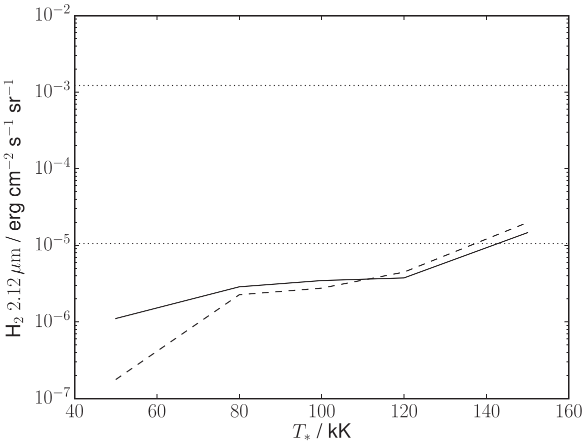

Figure 10. H$_2$ 2.12 μm surface brightness versus T_*, for models with $n_\mathrm{H} = 10^5\,\mathrm{cm}^{-3}$, $\log g = 7.0$, and $L_* = 100\,\mathrm{L}_\odot$ (solid line) and $1000\,\mathrm{L}_\odot$ (dashed line) including the EUV flux. The dotted horizontal lines show the range of observed values from Hora et al. (1999).

the ArH$^+$ and HeH$^+$ lines are only slightly weaker than the detection limits taken from Aleman et al. (2014). Increasing $\log g$ to 8.0 reduces model surface brightnesses by at most a factor of a few compared to $\log g = 7.0$.

Figs 9 and 10 show, respectively, the predicted OH$^+$ 971 GHz and H$_2$ 2.12 μm line surface brightnesses versus T_*, for models including the EUV flux. Models with $T_* < 150\,\mathrm{kK}$ have much higher surface brightnesses in both lines than the corresponding models without the additional flux, as the EUV flux heats the gas at the edge of the knot to much higher temperatures, as well as increasing the ionization fraction. The H$_2$ 2.12 μm surface brightnesses are increased to within a factor of a few of observed values for $T_* \geq 80\,\mathrm{kK}$. As with H$_2$, for $T_* < 150\,\mathrm{kK}$ there is a significant increase in the OH$^+$ surface brightnesses. Models with $T_* > 80\,\mathrm{kK}$ all predict surface brightnesses similar to or higher than observations, while for $T_* = 50\,\mathrm{kK}$ the predicted values are below the lowest observed. Aleman et al. (2014) only detected OH$^+$ emission from PNe with $T_* \geq 100\,\mathrm{kK}$ – while our models in this temperature range are consistent with the observed surface brightness, we also predict similar values for $T_* = 80\,\mathrm{kK}$, whereas observations by Aleman et al. (2014) of three high-luminosity PNe with $80\,\mathrm{kK} \leq T_* < 100\,\mathrm{kK}$ did not detect any OH$^+$ lines. The reasons for this are discussed in Section 4.5. The CO J = 4–3 surface brightnesses are essentially unchanged from the previous values. Fig. 11 shows the ArH$^+$ 617 GHz surface brightnesses versus T_* for the models including the EUV flux. The $T_* = 150\,\mathrm{kK}$ models both predict surface brightnesses above the detection threshold, while for lower T_* the predicted values are much higher than the original case, although still consistent with the non-detection of this line in PNe. For HeH$^+$, the predicted 149 μm surface brightnesses are above the detection threshold for all models.

Fig. 12 shows the OH$^+$ column density versus T_* for models including the EUV flux. The column density is calculated by integrating through a single knot – multiple knots along the line of sight would result in higher values. The range of values in PNe calculated by Aleman et al. (2014) from observations, assuming lo-

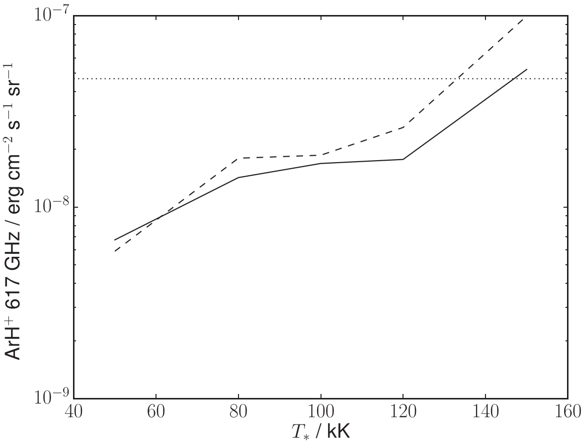

Figure 11. ArH$^+$ 617 GHz surface brightness versus T_*, for models with $n_H = 10^5$ cm^{-3}, $\log g = 7.0$, and $L_* = 100\,L_\odot$ (solid line) and $1000\,L_\odot$ (dashed line) including the EUV flux. The dotted horizontal line shows the surface brightness of the weakest SPIRE OH$^+$ detection from Aleman et al. (2014).

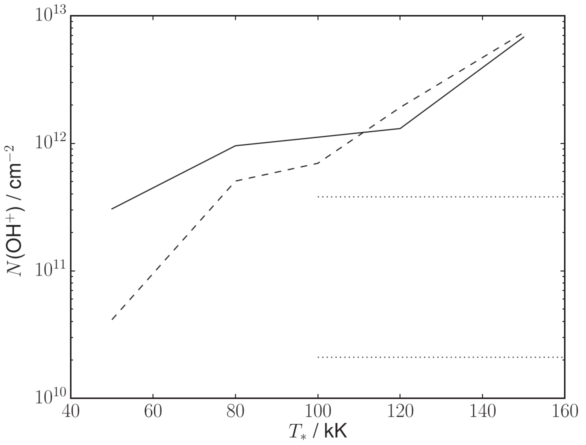

Figure 12. OH$^+$ column density versus T_*, for models with $n_H = 10^5$ cm^{-3}, $\log g = 7.0$, and $L_* = 100\,L_\odot$ (solid line) and $1000\,L_\odot$ (dashed line) including the EUV flux. The dotted horizontal lines show the range of values calculated from observations by Aleman et al. (2014).

cal thermodynamic equilibrium (LTE), are also shown. All models which reproduce the observed OH$^+$ line surface brightnesses have column densities significantly larger than those found by Aleman et al. (2014). Otsuka et al. (2017) found an OH$^+$ column density of 10^{13} cm^{-2} in their model of NGC 6781, also significantly higher than the value for this PN derived from observations. As we calculate the line emission directly, without assuming LTE, and since models without the EUV flux, which have lower OH$^+$ column densities, predict surface brightnesses below that observed, the higher values from our models are likely to be more accurate.

4 DISCUSSION

4.1 Location of the molecular emission

Fig. 13 shows the abundances of H, H$_2$, and e$^-$, and the gas temperature, versus distance into the knot for the 120 kK $100\,L_\odot$ UCL_PDR model including the EUV flux. At the edge of the knot the gas temperature and ionization fraction are high ($\sim10^4$K and $\sim$0.2, respectively). The ionization fraction decreases smoothly with distance as the EUV flux is rapidly attenuated, while the gas temperature drops much more sharply at a distance of $\sim2 \times 10^{14}$ cm. Aleman et al. (2011), who used similar values for the gas and central star properties, found similar temperatures and ionization fractions for their K1 model (with a step-function density profile), although the decrease in temperature is less sharp than in our models. The H$_2$ abundance rises slowly from an initial level of 10^{-4} before rapidly increasing at $\sim2 \times 10^{14}$ cm, with the PDR region where hydrogen is mostly atomic taking up a relatively small part of the knot. Aleman et al. (2011) stopped their models once the gas temperature reached 100 K – in this region, our models are in good agreement, although our H$_2$ abundances in the 100 K region are slightly lower.

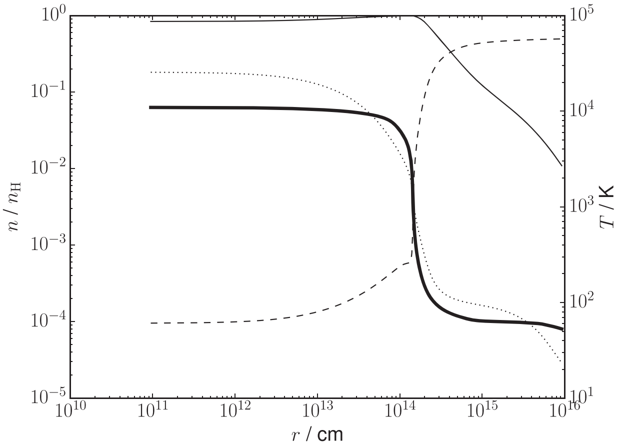

Figure 13. Abundances of H (thin solid line), H$_2$ (dashed line) and e$^-$ (dotted line) and gas temperature (thick solid line) versus distance into the knot for the 120 kK $100\,L_\odot$ $\log g = 7.0$ EUV model. The left y-axis shows the abundance relative to hydrogen nuclei, and the right shows the gas temperature.

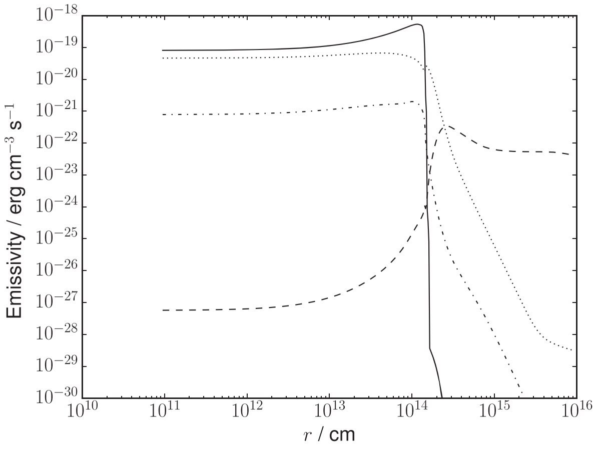

Figure 14. Line emissivities of H$_2$ 2.12 μm (solid line), CO J = 4–3 (dashed line), OH$^+$ 971 GHz (dotted line) and ArH$^+$ 617 GHz (dot–dashed line) versus distance into the knot for the 120 kK $100\,L_\odot$ $\log g = 7.0$ EUV model.

Fig. 14 shows the emissivities of the H$_2$ 2.12 μm, CO J = 4–3, OH$^+$ 971 GHz and ArH$^+$ 617 GHz lines versus distance. The 2.12 μm emission is concentrated in the ionized and PDR regions, despite the H$_2$ abundance not rising above 10^{-3}, and the emissivity is negligible in the molecular region of the knot as the much lower gas temperatures are unable to significantly populate the upper vibrational levels. Aleman et al. (2011) found similar peak emissivities for this line, although in our models the emissivity drops off much more sharply into the cloud, as with the temperature. The OH^+ and ArH^+ emissivities are also highest at the edge of the knot, but decrease more gradually than for H_2, with the emission extending into the molecular region. The CO J = 4–3 emissivity, unlike the other lines, is highest in the molecular region, with the contribution from the ionized/atomic parts of the knot negligible. Increasing L_* produces higher temperatures and ionization fractions, and a smaller molecular region, while the size of the molecular region increases with T_* as the FUV flux decreases.

4.2 Treatment of EUV flux

Our EUV models include, as part of the X-ray flux in UCL_PDR, the ionizing photon flux from 0.1−750 Å as X-rays in UCL_PDR. The 750−912 Å flux is absorbed in the ionized region treated by MOCASSIN. UCL_PDR uses the methods described by Meijerink & Spaans (2005) to treat X-rays, which are not designed with EUV photons in mind. The code calculates the wavelength-dependent cross-section for photoionization using the fits from Verner & Yakovlev (1995), and uses this to calculate the ionization and heating rates at each point in the knot. As the fits are not limited to X-ray wavelengths, the contribution to the ionization and gas heating by the EUV radiation will be correctly included. However, the chemical network only includes singly and doubly ionized elements, and of these, only cooling by C^+, Si^+, and Fe^+ is accounted for. The cooling rate is therefore likely to be underestimated, and the model gas temperature is likely too high.

Molecular photodissociation rates are based on the UMIST data base (McElroy et al. 2013) rates, scaled by the ratio of the energy density between 912 and 2400 Å to that of the Draine field (Draine 1978), and so does not include the effects of EUV photons. Significantly for our results, OH^+ (Saxon & Liu 1986), ArH^+ (Roueff, Alekseyev & Le Bourlot 2014), and HeH^+ (Roberge & Dalgarno 1982) all have photodissociation cross-sections which peak at EUV wavelengths. The EUV flux is also not included in the treatments of dust heating and gas heating by the dust photoelectric (PE) effect, which may be important in the deeper regions of our models where the dust PE effect is the dominant heating mechanism.

EUV photons are attenuated rapidly in the knots – in both MOCASSIN and UCL_PDR the flux at these wavelengths is reduced to zero within $\sim 10^{-4}$ pc, so the effects are only significant in the outer regions of the knot (corresponding to the transition zones in Aleman & Gruenwald 2011). As the CO emission originates from the PDR regions deeper into the knots, we do not expect those values to be sensitive to the EUV treatment – the differences between models with and without EUV are minimal. For the other molecules, the effects of including EUV are much more significant as the majority of the emission originates in the transition zones. In these parts of the knots, the heating rate is dominated by the X-ray/EUV flux, so the PE effect can be neglected. The main coolant in our models in these regions is atomic hydrogen – assuming that this would be the case even if cooling from all atomic/ionic species were included, we can be reasonably confident in the calculated temperatures in these regions.

The main issue with our treatment of the EUV flux is therefore the neglect of photodissociation by EUV photons, which will only have a significant impact if it is the main destruction mechanism for a particular molecule. Aleman & Gruenwald (2004) and Aleman et al. (2011) found charge exchange to be more significant in the destruction of H_2 in the transition zones of PNe, and as photodissociation by FUV photons, longwards of 912 Å, is accounted for, our H_2 abundances are unlikely to be strongly affected. For OH^+, ArH^+, and HeH^+, the increased photodissociation cross-sections in the EUV region (compared to the FUV) means that the photodissociation rates used are lower than the true values, and therefore the molecular abundances and the line emission will be overestimated. The extent will depend on the rates of other destruction mechanisms – in the transition zones, dissociative recombination with electrons is likely to be the most important destruction mechanism for the molecular ions, and if this is significantly higher than the photodissociation rates the effect on the abundances will be minimal.

4.3 Effect of input parameters

We have not investigated changing the values of a number of input parameters, including the dust-to-gas ratio, cosmic ray ionization rate, and the distance of the knot from the ionizing source, r_k, from their 'standard' values, all of which may affect the resulting molecular emission. Aleman et al. (2011) found that increasing the dust-to-gas mass ratio by an order of magnitude resulted in a ∼20 per cent increase in H_2 2.12 μm surface brightness in their models of cometary knots in NGC 7293. As this increase is most likely due to the increased H_2 formation rate on dust grains (Aleman & Gruenwald 2011), other molecules are unlikely to be as strongly affected, and it is not enough to remove the need for the EUV flux. Similarly, we find increasing the cosmic ray ionization rate by a factor of 100 has little effect except for a moderate increase in the OH^+ surface brightness for the lowest T_* models – with the inclusion of the EUV flux, the effects are negligible in all models.

Aleman et al. (2011) also found that r_k has an impact on the H_2 emission, which presumably applies to other molecules as well. The results shown in Aleman et al. (2011) suggest that the H_2 surface brightness (for a given set of knot parameters) does not vary enormously with distance, unless the knot is beyond the ionization front, at which point it decreases rapidly. Our value of $r_k = 0.2$ pc is within the nebular ionization front radius for all central star parameters investigated. Reducing r_k to 0.1 pc for the 100 $L_\odot$ 120 kK model, we find the H_2, OH^+, ArH^+, and HeH^+ surface brightnesses all increase by a factor of ∼2, while the CO surface brightness decreases by a similar factor. Aleman et al. (2011) also found that in some cases the H_2 surface brightness decreases with r_k below a certain radius, presumably due to the increased UV flux dissociating the molecules. This behaviour might also be expected for OH^+, ArH^+, and HeH^+, although as discussed in Section 4.2, this is not treated in our models due to the non-inclusion of EUV photodissociation for these molecules.

4.4 Shock heating and fluorescent emission

With the inclusion of EUV photons, our models predict H_2 surface brightnesses for $T_* \geq 80$ kK within a factor of a few of the lowest values observed in PNe (Hora et al. 1999). However, H_2 2.12 μm emission is observed in PNe with a much wider range of central star temperatures, down to 48 kK for NGC 40 (Hora et al. 1999; Ueta et al. 2014), and many PNe have surface brightnesses far higher than the values we obtain. This suggests that an additional source of H_2 emission is present in actual PNe which is missing from our models.

We assume that the PN knots are in thermal equilibrium, with the heating from the incident radiation field balanced by cooling from line emission and gas–grain interactions. H_2 emission can, however, be produced in the shocked region produced by the interaction of nebular material with the AGB wind from earlier evolutionary stages (Natta & Hollenbach 1998), in which case the gas may be heated to higher temperatures. Otsuka et al. (2017) proposed that the H_2 emission from NGC 6781 – one of the PNe with an OH^+ detection – is in fact due to shock heating, which they modelled by setting a minimum gas temperature. Table 4 lists observed molecular line surface brightnesses for NGC 6781 and NGC 7293, a PN with similar central star properties to those used by Otsuka et al. (2017, 100 $L_\odot$, 120 kK; Henry, Kwitter & Dufour 1999) but with H_2 emission which does not appear to be caused by shocks (O'Dell et al. 2007), along with predicted values from three PDR models with these central star parameters – our initial model (without any incident EUV radiation), the same model including the EUV flux and a model with both EUV flux and a minimum temperature $T_{\rm min} = 1500$ K (Otsuka et al. 2017 used $T_{\rm min} = 1420$ K for NGC 6781).

The initial model fails to reproduce the observed surface brightness of any line for both PNe, although the values for ArH^+ and HeH^+ are consistent with the non-detection of these lines. The EUV model is at worst within a factor of a few of observed surface brightnesses in NGC 7293 for H_2, CO, and OH^+, but predicts much lower H_2 and CO surface brightnesses than observed in NGC 6781. Aleman et al. (2011) also modelled the H_2 emission from the cometary knots in NGC 7293, and found surface brightnesses in good agreement with observed values, without incorporating shock heating, assuming the knot is seen edge on and integrating the peak emissivity over knot depths of order ∼0.001 pc. If we adopt this approach, rather than integrating the emissivity through the knot, we find a 2.12 μm surface brightness of 1.3×10^{-5} erg cm^{-2} s^{-1} sr^{-1}, within the range of observed values. The $T_{\rm min}$ model predicts H_2 and OH^+ surface brightnesses somewhat higher than observed in NGC 6871, while the CO J = 4–3 line is ∼100 times stronger than observed. The H_2 surface brightness is significantly higher than for NGC 7293 and for all of our other models, and is of the same order as the highest values observed in PNe (Hora et al. 1999), suggesting that the emission from these objects may originate from shocked gas. Akras, Gonçalves & Ramos-Larios (2017) found higher H_2 surface brightnesses (up to 10^{-3} erg cm^{-2} s^{-1} sr^{-1}) in K 4 – 47, which they suggest shows evidence of shock interactions. The ArH^+ and HeH^+ surface brightnesses are unchanged by the imposition of a minimum temperature. The ArH^+ 617 GHz surface brightness is below the detection threshold for both models, while the HeH^+ 149 μm surface brightness is higher.

An alternative excitation mechanism for H_2 line emission is fluorescence following the absorption of UV photons (Sternberg & Dalgarno 1989), a mechanism which is not treated by UCL_PDR. O'Dell et al. (2007) found that in the case of NGC 7293, fluorescence caused by non-ionizing UV photons (in the range 912−1100 Å) is an implausible mechanism for producing the observed H_2 emission, as too great a proportion of the flux must be reprocessed. For $\log g = 7.0$, the $T_* = 50$ kK model atmosphere emits the highest proportion of its flux in this range, about 0.14, while for higher T_* this decreases to $\lesssim$0.03. The unattenuated flux at 0.2 pc from a 100 $L_\odot$ central star is 0.08 erg cm^{-2} s^{-1}, so the maximum possible energy available to power fluorescence for $T_* = 50$ kK is 0.01 erg cm^{-2} s^{-1}. A 2.12 μm line surface brightness of 10^{-5} erg cm^{-2} s^{-1} sr^{-1} (the lowest observed values from Hora et al. 1999) would require ∼10^{-4} erg cm^{-2} s^{-1} if the emission is powered by fluorescence, corresponding to only 1 per cent of the available flux, suggesting that H_2 emission from PN with $T_* \lesssim 100$ kK could plausibly originate from this mechanism. For higher T_*, the lower flux in the range producing fluorescence means that the criticisms of O'Dell et al. (2007) still stand, and the highest H_2 surface brightnesses observed in PNe seem incapable of being produced by this mechanism.

4.5 Non-detections of OH^+

In the sample of Aleman et al. (2014), all the PNe with OH^+ detections have central star temperature $T_* \gtrsim 100$ kK. However, two PNe listed as having central star temperatures in this range, NGC 7027 and Mz 3, are not detected in OH^+. Aleman et al. (2014) suggested that the high (2.3) C/O ratio in NGC 7027 may explain the non-detection of OH^+, as the available oxygen is locked up in CO molecules. Increasing the carbon abundance and reducing the oxygen abundance to 6×10^{-4} and 2×10^{-4}, respectively, our 100 $L_\odot$, 120 kK model predicts an OH^+ surface brightness of 2.4×10^{-7} erg cm^{-2} s^{-1} sr^{-1}, only slightly reduced from the original value of 6.6×10^{-7} erg cm^{-2} s^{-1} sr^{-1}. This reflects the lower oxygen abundance rather than any locking-up of the oxygen, as the OH^+ emission originates in the ionized/PDR region where the CO abundance is low. The lack of observed OH^+ emission in NGC 7027 is therefore unlikely to be due to the C/O ratio, and may instead be due to the smaller nebular radius (0.03 pc compared to ∼0.1 pc for PNe with OH^+ detections), and its very high central star luminosity (10^4 $L_\odot$; Middlemass 1990) which would imply a much higher flux of UV photons in the knot and therefore a higher photodissociation rate for OH^+. This could also account for the non-detection of ArH^+ and HeH^+ in this PN, which was in apparent conflict with the predictions of our models. Mz 3 was listed by Aleman et al. (2014) as having $T_* = 107$ kK, citing Phillips (2003). However, a number of other authors have estimated a much lower central star temperature of 32−36 kK (Cohen et al. 1978; Zhang & Liu 2002; Smith 2003), for which our models predict no detectable OH^+ emission.

Our models with $T_* = 80$ kK predict OH^+ surface brightnesses similar to those with $T_* = 100$ kK. However, of the three PNe listed by Aleman et al. (2014) as having T_* in the range of 80−90 kK, none have OH^+ detections. All three PNe (NGC 3242, NGC 7009 and NGC 7026) are highly luminous ($L_* \sim 2000−5000$ $L_\odot$; Frew 2008), and have ionized radii of ∼0.1 pc, smaller than assumed in our low-luminosity models, so the increase in the UV flux, and therefore the photodissociation rates, will be very substantial, accounting for their lack of detectable molecular line emission.

4.6 ArH^+ and HeH^+ emission

Our EUV models all predict HeH^+ surface brightnesses at or above detection thresholds, and our models with $T_* = 150$ kK also predict detectable levels of ArH^+ emission, despite neither molecule having yet been detected in PNe. HeH^+ has previously been predicted to form in detectable quantities in PNe (e.g. Cecchi-Pestellini & Dalgarno 1993), while ArH^+ is known to be present in mainly atomic regions with low H_2 abundances and a suitable ionization source (Schilke et al. 2014; Priestley et al. 2017), conditions which certainly apply to the surface regions of knots in PNe.

In models for the clumps in the Crab nebula (Priestley et al. 2017), it was found that the predicted equilibrium level of HeH^+ emission was large enough to have been detected in *Herschel* PACS spectra. However, the formation time-scale for HeH^+ was found to be significantly larger than the age of the Crab, suggesting that the assumption of chemical equilibrium can lead to an overestimate for the molecule's abundance. The formation time-scale for ArH^+, by contrast, is short enough that the assumption of equilibrium is justified. Fig. 15 shows the formation time-scales for HeH^+, OH^+, and ArH^+ versus distance into a knot at a distance of 0.2 pc, for

Table 4. Observed line surface brightnesses for NGC 7293 and NGC 6781, and models with $L_* = 100\,L_\odot$ and $T_* = 120$ kK. Details of models are described in the text. Surface brightnesses are in $\mathrm{erg\,cm^{-2}\,s^{-1}\,sr^{-1}}$. Observed values are from Aleman et al. (2011, H_2) and Etxaluze et al. (2014, CO, OH^+, ArH^+) for NGC 7293, and Otsuka et al. (2017, H_2, CO) and Aleman et al. (2014, OH^+, ArH^+, HeH^+) for NGC 6871.

Model	H_2 2.12 µm	CO J = 4–3	OH^+ 971 GHz	ArH^+ 617 GHz	HeH^+ 149 µm
NGC 7293	$0.9{-}3.7 \times 10^{-5}$	$0.7{-}2.0 \times 10^{-7}$	$4.1{-}9.3 \times 10^{-7}$	$\lesssim 4 \times 10^{-8}$	–
NGC 6781	2.7×10^{-4}	3.7×10^{-7}	$4.3{-}4.7 \times 10^{-7}$	$\lesssim 5 \times 10^{-8}$	$\lesssim 9 \times 10^{-7}$
Initial	7.7×10^{-17}	3.4×10^{-8}	4.2×10^{-10}	2.5×10^{-12}	9.5×10^{-12}
EUV	3.8×10^{-6}	4.2×10^{-8}	6.6×10^{-7}	1.8×10^{-8}	2.1×10^{-6}
T_{min}	9.0×10^{-4}	2.3×10^{-5}	1.1×10^{-6}	1.8×10^{-8}	2.1×10^{-6}

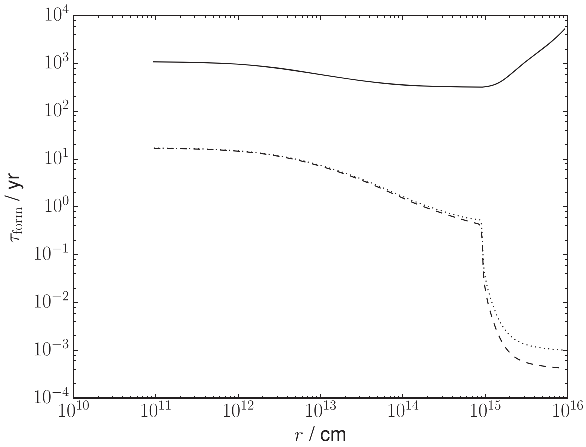

Figure 15. Formation time-scales versus distance into the knot for HeH^+ (solid line), OH^+ (dashed line), and ArH^+ (dotted line), for the 150 kK $1000\,L_\odot$ $\log g = 7.0$ EUV model.

the 150 kK, $1000\,L_\odot$ EUV model. The abundances of all three molecules drop off beyond $\sim 10^{15}$ cm, which combined with the lower temperature means that there is no significant emission beyond this point. The formation time-scales in this region for ArH^+ and OH^+ are similar, of order a few to 10 yr, whereas for HeH^+ the time-scale is much larger ($\tau_{\mathrm{form}} \sim 300{-}1000$ yr). Given typical ages of these old PNe (>1000 yr; Ueta et al. 2014), this is unlikely to be long enough to significantly reduce the abundance of these species. A possible explanation is the EUV field – as discussed in Section 4.2, photodissociation by EUV photons is not treated by our models. The inclusion of the EUV flux would therefore be expected to reduce the abundances of both molecules, potentially reducing the emission to below the detection threshold.

5 CONCLUSIONS

We have performed combined photoionization and PDR modelling of PN cometary knots, for a range of central star parameters and gas densities. Our initial PDR models fail to reproduce the observed H_2 and OH^+ surface brightnesses for PNe with $T_* < 150$ kK. Only by including the ionizing UV flux from the central star do the models predict surface brightnesses for $T_* \geq 100$ kK consistent with the values observed in PNe. Predicted OH^+ column densities are $\gtrsim 10^{12}\,\mathrm{cm^{-2}}$, significantly larger than those derived from observations assuming LTE, but in agreement with previous modelling work (Otsuka et al. 2017). Predicted H_2 surface brightnesses are somewhat lower than observed values, and our models do not explain the highest emission strengths observed in PNe, or the detection of H_2 emission in PNe with cooler ($T_* < 80$ kK) central stars. The presence of shocks may be capable of producing the higher H_2 surface brightnesses observed, while fluorescence due to excitation by UV photons could be a viable source of H_2 emission for nebulae with central star temperatures below 50 kK. Our models predict HeH^+ (and, for $T_* = 150$ kK, ArH^+) line surface brightnesses potentially above detection thresholds, despite neither molecule having been detected in PNe. As photodissociation by EUV photons is not treated for either molecule, the true surface brightnesses may be significantly lower than our predicted values if this is an important destruction mechanism.

ACKNOWLEDGEMENTS

FP is supported by the Perren fund and UCL IMPACT fund. MJB acknowledges support from the European Research Council grant SNDUST ERC-2015-AdG-694520. We would like to thank Prof. Jonathan Tennyson for providing the recent ArH^+ dissociative recombination rates of Abdoulanziz et al. The TheoSSA service (http://dc.g-vo.org/theossa) used to retrieve theoretical spectra for this paper was constructed as part of the activities of the German Astrophysical Virtual Observatory.

REFERENCES

Akras S., Gonçalves D. R., Ramos-Larios G., 2017, MNRAS, 465, 1289
Aleman I., Gruenwald R., 2004, ApJ, 607, 865
Aleman I., Gruenwald R., 2011, A&A, 528, A74
Aleman I., Zijlstra A. A., Matsuura M., Gruenwald R., Kimura R. K., 2011, MNRAS, 416, 790
Aleman I. et al., 2014, A&A, 566, A79
Bachiller R., Huggins P. J., Cox P., Forveille T., 1993, A&A, 267, 177
Barlow M. J. et al., 2013, Science, 342, 1343
Bayet E., Williams D. A., Hartquist T. W., Viti S., 2011, MNRAS, 414, 1583
Bell T. A., Viti S., Williams D. A., Crawford I. A., Price R. J., 2005, MNRAS, 357, 961
Bell T. A., Roueff E., Viti S., Williams D. A., 2006, MNRAS, 371, 1865
Cecchi-Pestellini C., Dalgarno A., 1993, ApJ, 413, 611
Cohen M., Kunkel W., Lasker B. M., Osmer P. S., Fitzgerald M. P., 1978, ApJ, 221, 151
Draine B. T., 1978, ApJS, 36, 595
Edwards J. L., Cox E. G., Ziurys L. M., 2014, ApJ, 791, 79
Ercolano B., Barlow M. J., Storey P. J., Liu X.-W., 2003, MNRAS, 340, 1136
Ercolano B., Barlow M. J., Storey P. J., 2005, MNRAS, 362, 1038
Ercolano B., Young P. R., Drake J. J., Raymond J. C., 2008, ApJS, 175, 534
Etxaluze M. et al., 2014, A&A, 566, A78
Frew D. J., 2008, PhD thesis, Macquarie University
Guerrero M. A., De Marco O., 2013, A&A, 553, A126
Habing H. J., 1968, Bull. Astron. Inst. Netherlands, 19, 421
Henry R. B. C., Kwitter K. B., Dufour R. J., 1999, ApJ, 517, 782
Hiriart D., 2005, A&A, 434, 181
Hora J. L., Latter W. B., Deutsch L. K., 1999, ApJS, 124, 195
Huggins P. J., Bachiller R., Cox P., Forveille T., 1996, A&A, 315, 284
Jenkins E. B., 2009, ApJ, 700, 1299

Kimura R. K., Gruenwald R., Aleman I., 2012, A&A, 541, A112
Kingsburgh R. L., Barlow M. J., 1994, MNRAS, 271, 257
Lique F., Bulut N., Roncero O., 2016, MNRAS, 461, 4477
Lodders K., 2010, Astrophys. Space Sci. Proc., 16, 379
McElroy D., Walsh C., Markwick A. J., Cordiner M. A., Smith K., Millar T. J., 2013, A&A, 550, A36
Matsuura M. et al., 2007, MNRAS, 382, 1447
Matsuura M. et al., 2009, ApJ, 700, 1067
Meaburn J., Clayton C. A., Bryce M., Walsh J. R., Holloway A. J., Steffen W., 1998, MNRAS, 294, 201
Meijerink R., Spaans M., 2005, A&A, 436, 397
Middlemass D., 1990, MNRAS, 244, 294
Miller Bertolami M. M., 2016, A&A, 588, A25
Mufson S. L., Lyon J., Marionni P. A., 1975, ApJ, 201, L85
Natta A., Hollenbach D., 1998, A&A, 337, 517
Neufeld D. A., Wolfire M. G., 2017, ApJ, 845, 163
O'Dell C. R., Handron K. D., 1996, AJ, 111, 1630
O'Dell C. R., Balick B., Hajian A. R., Henney W. J., Burkert A., 2002, AJ, 123, 3329
O'Dell C. R., Henney W. J., Ferland G. J., 2007, AJ, 133, 2343
Osterbrock D. E., Ferland G. J., 2006, Astrophysics of Gaseous Nebulae and Active Galactic Nuclei. University Science Books, Mill Valley, CA
Otsuka M. et al., 2017, ApJS, 231, 22
Phillips J. P., 2003, MNRAS, 344, 501
Pottasch S. R., Beintema D. A., Feibelman W. A., 2005, A&A, 436, 953
Priestley F. D., Barlow M. J., Viti S., 2017, MNRAS, 472, 4444
Rauch T., 2003, A&A, 403, 709
Roberge W., Dalgarno A., 1982, ApJ, 255, 489
Roueff E., Alekseyev A. B., Le Bourlot J., 2014, A&A, 566, A30
Saxon R. P., Liu B., 1986, J. Chem. Phys., 85, 2099
Schilke P. et al., 2014, A&A, 566, A29
Schmidt D. R., Ziurys L. M., 2016, ApJ, 817, 175
Smith N., 2003, MNRAS, 342, 383
Sternberg A., Dalgarno A., 1989, ApJ, 338, 197
Tielens A. G. G. M., Hollenbach D. J., 1993, in Weinberger R., Acker A., eds, Proc. IAU Symp. 155, Planetary Nebulae. Kluwer, Dordrecht. p. 155
Treffers R. R., Fink U., Larson H. P., Gautier T. N., III, 1976, ApJ, 209, 793
Ueta T. et al., 2014, A&A, 565, A36
van der Tak F. F. S., Nagy Z., Ossenkopf V., Makai Z., Black J. H., Faure A., Gerin M., Bergin E. A., 2013, A&A, 560, A95
van der Werf P. P. et al., 2010, A&A, 518, L42
Vassiliadis E., Wood P. R., 1994, ApJS, 92, 125
Verner D. A., Yakovlev D. G., 1995, A&AS, 109
Wyrowski F., Menten K. M., Güsten R., Belloche A., 2010, A&A, 518, A26
Zhang Y., Liu X.-W., 2002, MNRAS, 337, 499

This paper has been typeset from a TEX/LATEX file prepared by the author.